
Persistent Classification: Understanding Adversarial Attacks by Studying Decision Boundary Dynamics

Brian Bell

Department of Mathematics,
University of Arizona
Los Alamos National Laboratory
bwbell@lanl.gov

Michael Geyer

Department of Computer Science,
University of Texas San Antonio
Los Alamos National Laboratory
mgeyer@lanl.gov

David Glickenstein

Department of Mathematics,
University of Arizona

Keaton Hamm

Division of Data Science,
University of Texas at Arlington

Carlos Scheidegger

Department of Computer Science,
University of Arizona

Amanda Fernandez

Department of Computer Science
University of Texas San Antonio

Juston Moore

Los Alamos National Laboratory

Abstract

There are a number of hypotheses underlying the existence of adversarial examples for classification problems. These include the high-dimensionality of the data, high codimension in the ambient space of the data manifolds of interest, and that the structure of machine learning models may encourage classifiers to develop decision boundaries close to data points. This article proposes a new framework for studying adversarial examples that does not depend directly on the distance to the decision boundary. Similarly to the smoothed classifier literature, we define a (natural or adversarial) data point to be (γ, σ) -stable if the probability of the same classification is at least γ for points sampled in a Gaussian neighborhood of the point with a given standard deviation σ . We focus on studying the differences between persistence metrics along interpolants of natural and adversarial points. We show that adversarial examples have significantly lower persistence than natural examples for large neural networks in the context of the MNIST and ImageNet datasets. We connect this lack of persistence with decision boundary geometry by measuring angles of interpolants with respect to decision boundaries. Finally, we connect this approach with robustness by developing a manifold alignment gradient metric and demonstrating the increase in robustness that can be achieved when training with the addition of this metric.

The idea of expanding Gaussian perturbations around a data point has been studied previously as smoothed classifiers. Whereas Roth et al. [44] consider adding various types of noise to a given point and Hosseini et al. [19] consider small Gaussian perturbations of x sampled from $N(x, \varepsilon^2 I)$ for small ε , we specifically focus on tuning the standard deviation parameter to determine a statistic describing how a given data point is placed within its class. The γ -persistence then gives a measurement similar to distance to the boundary but that is drawn from sampling instead of distance. This sampling allows for a better description of the local geometry of the class and decision boundary, as we will see in Section 3.1. Our statistic is based on the fraction of a Gaussian sampling of the neighborhood of a

point that receives the same classification; this is different from that of Roth et al. [44], which is the expected error of the original data points logit and the perturbed data points logit. Additionally, while their statistics are defined pairwise with reference to pre-chosen original and candidate classes, ours is not.

1 Introduction

Deep Neural Networks (DNNs) and their variants are core to the success of modern machine learning [42], and have dominated competitions in image processing, optical character recognition, object detection, video classification, natural language processing, and many other fields [46]. Yet such classifiers are notoriously susceptible to manipulation via adversarial examples [52]. Adversarial examples occur when natural data can be subject to subtle perturbation which results in substantial changes in output. Adversarial examples are not just a peculiarity, but seem to occur for most, if not all, DNN classifiers. For example, Shafahi et al. [47] used isoperimetric inequalities on high dimensional spheres and hypercubes to conclude that there is a reasonably high probability that a correctly classified data point has a nearby adversarial example. This has been reiterated using mixed integer linear programs to rigorously check minimum distances necessary to achieve adversarial conditions [54]. In addition, Ilyas et al. [21] showed that adversarial examples can arise from features that are good for classification but not robust to perturbation.

There have been many attempts to identify adversarial examples using properties of the decision boundary. Fawzi et al. [13] found that decision boundaries tend to have highly curved regions, and these regions tend to favor negative curvature, indicating that regions that define classes are highly non-convex. The purpose of this work is to investigate these geometric properties related to the decision boundaries. We will do this by proposing a notion of stability that is more nuanced than simply measuring distance to the decision boundary, and is also capable of elucidating information about the curvature of the nearby decision boundary. We develop a statistic extending prior work on smoothed classifiers by Cohen et al. [9]. We denote this metric as Persistence and use it as a measure of how far away from a point one can go via Gaussian sampling and still consistently find points with the same classification. One advantage of this statistic is that it is easily estimated by sending a Monte Carlo sampling about the point through the classifier. In combination with this metric, direct measurement of decision boundary incidence angle with dataset interpolation and manifold alignment can begin to complete the picture for how decision boundary properties are related with neural network robustness.

These geometric properties are related to the alignment of gradients with human perception [15, 24, 48] and with the related underlying manifold [24, 21] which may imply robustness. For our purposes, Manifold Aligned Gradients (MAG) will refer to the property that the gradients of a model with respect to model inputs follow a given data manifold \mathcal{M} extending similar relationships from other work by Shamir et al. [50].

Contributions. We believe these geometric properties are related to why smoothing methods have been useful in robustness tasks [9, 33, 35]. We propose three approaches in order to connect robustness with geometric properties of the decision boundary learned by DNNs:

1. We propose and implement two metrics based on the success of smoothed classification techniques: (γ, σ) -stability and γ -persistence defined with reference to a classifier and a given point (which can be either a natural or adversarial image, for example) and demonstrate their validity for analyzing adversarial examples.
2. We interpolate across decision boundaries using our persistence metric to demonstrate an inconsistency at the crossing of a decision boundary when interpolating from natural to adversarial examples.
3. We demonstrate via direct interpolation across decision boundaries and measurement of angles of interpolating vectors relative to the decision boundary itself that dimensionality is not solely responsible for geometric vulnerability of neural networks to adversarial attack.

2 Motivation and related work

Our work is intended to shed light on the existence and prevalence of adversarial examples to DNN classifiers. It is closely related to other attempts to characterize robustness to adversarial perturbations, and here we give a detailed comparison.

Distance-based robustness.

A typical approach to robustness of a classifier is to consider distances from the data manifold to the decision boundary [60, 62, 18]. Khoury and Hadfield-Menell [25] define a classifier to be robust if the class of each point in the data manifold is contained in a sufficiently large ball that is entirely contained in the same class. The larger the balls, the more robust the classifier. It is then shown that if training sets are sufficiently dense in relation to the reach of the decision axis, the classifier will be robust in the sense that it classifies nearby points correctly. In practice, we do not know that the data is so well-positioned, and it is quite possible, especially in high dimensions, that the reach is extremely small, as evidenced by results on the prevalence of adversarial examples, e.g., Shafahi et al. [47] and in evaluation of ReLU networks with mixed integer linear programming e.g., Tjeng et al. [54].

Tsipras et al. [58] investigated robustness in terms of how small perturbations affect the the average loss of a classifier. They define standard accuracy of a classifier in terms of how often it classifies correctly, and robust accuracy in terms of how often an adversarially perturbed example classifies correctly. It was shown that sometimes accuracy of a classifier can result in poor robust accuracy. Gilmer et al. [16] use the expected distance to the nearest different class, when drawing a data point from the data distribution, to capture robustness. They then show that an accurate classifier can result in a small distance to the nearest different class in high dimensions when the data is drawn from concentric spheres. Many recent works [18, 8, 22] have linked robustness with decision boundary dynamics, both by augmenting training with data near decision boundaries, or with dynamics related to distances from decision boundaries. We acknowledge the validity of this work, but will address some of its primary limitations by carefully studying the orientation of the decision boundary relative to model data.

A related idea is that adversarial examples often arise within cones, outside of which images are classified in the original class, as observed by Roth et al. [44]. Many theoretical models of adversarial examples, for instance the dimple model developed by Shamir [49], have high curvature and/or sharp corners as an essential piece of why adversarial examples can exist very close to natural examples.

Adversarial detection via sampling. While adversarial examples often occur, they still may be rare in the sense that most perturbations do not produce adversarial examples. Hu et al. [20] used the observation that adversarial examples are both rare and close to the decision boundary to detect adversarial examples. They take a potential data point and look to see if nearby data points are classified differently than the original data point after only a few iterations of a gradient descent algorithm. If this is true, the data point is likely natural and if not, it is likely adversarial. This method has been generalized with the developing of smoothed classification methods [9, 33, 35] which at varying stages of evaluation add noise to the effect of smoothing output and identifying adversaries due to their higher sensitivity to perturbation.. These methods suffer from significant computational complexity [29] and have been shown to have fundamental limitations in their ability to rigorously certify robustness [5, 63]. We will generalize this approach into a metric which will allow us to directly study these limitations in order to better understand how geometric properties have given rise to adversarial vulnerabilities. In general, the results of Hu et al. [20] indicate that considering samples of nearby points, which approximate the computation of integrals, is likely to be more successful than methods that consider only distance to the decision boundary.

Roth et al. [44] proposed a statistical method to identify adversarial examples from natural data. Their main idea was to consider how the last layer in the neural network (the logit layer) would behave on small perturbations of a natural example. This is then compared to the behavior of a potential adversarial example.

It was shown by Hosseini et al. [19] that it is possible to produce adversarial examples, for instance using a logit mimicry attack, that instead of perturbing an adversarial example toward the true class, actually perturb to some other background class. In fact, we will see in Section 4.1.1 that the emergence of a background class, which was observed as well by Roth et al. [44], is quite common.

Although many recent approaches have taken advantage of these facts [53, 37, 41, 4] in order to measure and increase robustness, we will leverage these sampling properties to develop a metric directly on decision-boundary dynamics and how they relate to the success of smoothing based robustness.

Manifold Aware Robustness

The sensitivity of convolutional neural networks to imperceptible changes in input has thrown into question the true generalization of these models. Jo and Bengio [23] study the generalization performance of CNNs by transforming natural image statistics. Similarly to our MAG approach, they create a new dataset with well-known properties to allow the testing of their hypothesis. They show that CNNs focus on high level image statistics rather than human perceptible features. This problem is made worse by the fact that many saliency methods fail basic sanity checks [1, 27].

Until recently, it was unclear whether robustness and manifold alignment were directly linked, as the only method to achieve manifold alignment was adversarial training. Along with the discovery that smoothed classifiers are perceptually aligned, comes the hypothesis that robust models in general share this property put forward by Kaur et al. [24]. This discovery raises the question of whether this relationship between manifold alignment of model gradients and robustness is bidirectional.

Khoury and Hadfield-Menell [25] study the geometry of natural images, and create a lower bound for the number of data points required to effectively capture variation in the manifold. They demonstrate that this lower bound is so large as to be intractable for all practical datasets, severely limiting robustness guarantees that rely on sampling from the data distribution. Vardi et al. [59] demonstrate that even models that satisfy strong conditions related to max margin classifiers are implicitly non-robust. Instead of relying on sampling, Shamir et al. [50] propose using the tangent space of a generative model as an estimation of this manifold. This approach reduces the sampling requirements; however, this approach relies on a generative model which will, by definition, suffer from the same dimensionality limitations. On the other hand, Magai and Ayzenberg [39] thoroughly review certain topological properties to demonstrate that neural networks intrinsically use relatively few dimensions of variation during training and evaluation. It is possible that the this ability to reduce degrees of freedom is the mechanism which resolves the curse of dimensionality inherent to many deep learning problems, especially when domain specific constraints are used to define the data manifold. PCA and manifold metrics have been recently used to identify adversarial examples [2, 40]. We will extend this work to study the relationship between robustness and manifold alignment directly by baking alignment directly into networks and comparing them with other forms of robustness.

Summary. In Sections 3 and 4, we will investigate stability of both natural data and adversarial examples by considering sampling from Gaussian distributions centered at a data point with varying standard deviations. Using the standard deviation as a parameter, we are able to derive a statistic for each point that captures how entrenched it is in its class in a way that is less restrictive than the robustness described by Khoury and Hadfield-Menell [25], takes into account the rareness of adversarial examples described by Hu et al. [20], builds on the idea of sampling described by Roth et al. [44] and Hosseini et al. [19], and represent curvatures in a sense related to Fawzi et al. [13]. Furthermore, we will relate these stability studies to direct measurement of interpolation incident angles with decision boundaries in Subsection 3.2 and 4.3 and the effect of reduction of data onto a known lower dimensional manifold in Subsections 4.5 and 4.4.

3 Methods

In this section we will lay out the theoretical framework for studying stability, persistence, and decision boundary crossing-angles.

3.1 Stability and Persistence

In this section we define a notion of stability of classification of a point under a given classification model. In the following, X represents the ambient space the data is drawn from (typically \mathbb{R}^n) even if the data lives on a sub-manifold of X , and L is a set of labels (often $\{1, \dots, \ell\}$). Note that points $x \in X$ can be natural or adversarial points.

Definition 3.1. Let $\mathcal{C} : X \rightarrow L$ be a classifier, $x \in X$, $\gamma \in (0, 1)$, and $\sigma > 0$. We say x is (γ, σ) -stable with respect to \mathcal{C} if $\mathbb{P}[\mathcal{C}(x') = \mathcal{C}(x)] \geq \gamma$ for $x' \sim \rho = N(x, \sigma^2 I)$; i.e. x' is drawn from a Gaussian with variance σ^2 and mean x .

In the common setting when $X = \mathbb{R}^n$, we have

$$\mathbb{P}[\mathcal{C}(x') = \mathcal{C}(x)] = \int_{\mathbb{R}^n} \mathbb{1}_{\mathcal{C}^{-1}(\mathcal{C}(x))}(x') d\rho(x') = \rho(\mathcal{C}^{-1}\mathcal{C}(x)).$$

Note here that \mathcal{C}^{-1} denotes pre-image. One could substitute various probability measures ρ above with mean x and variance σ^2 to obtain different measures of stability corresponding to different ways of sampling the neighborhood of a point. Another natural choice would be sampling the uniform measure on balls of changing radius. Based on the concentration of measure for both of these families of measures we do not anticipate significant qualitative differences in these two approaches. We propose Gaussian sampling because it is also a product measure, which makes it easier to sample and simplifies some of our calculations. Figure 1 below compares the uniform measure on balls with our γ -softened approach and its insensitivity to rare events which in this case highlights more macro-scale features which would be missed by a hard ball.

For the Gaussian measure, the probability above may be written more concretely as

$$\frac{1}{(\sqrt{2\pi}\sigma)^n} \int_{\mathbb{R}^n} \mathbb{1}_{\mathcal{C}^{-1}(\mathcal{C}(x))}(x') e^{-\frac{|x-x'|^2}{2\sigma^2}} dx'. \quad (1)$$

In this work, we will conduct experiments in which we estimate this stability for fixed (γ, σ) pairs via a Monte Carlo sampling, in which case the integral (1) is approximated by taking N i.i.d. samples $x_k \sim \rho$ and computing

$$\frac{|x_k : \mathcal{C}(x_k) = \mathcal{C}(x)|}{N}.$$

Note that this quantity converges to the integral (1) as $N \rightarrow \infty$ by the Law of Large Numbers.

The ability to adjust the quantity γ is important because it is much weaker than a notion of stability that requires a ball that stays away from the decision boundary as by Khoury and Hadfield-Menell [25]. By choosing γ closer to 1, we can require the samples to be more within the same class, and by adjusting γ to be smaller we can allow more overlap.

We also propose a related statistic, *persistence*, by fixing a particular γ and adjusting σ . For any $x \in X$ not on the decision boundary, for any choice of $0 < \gamma < 1$ there exists a σ_γ small enough such that if $\sigma < \sigma_\gamma$ then x is (γ, σ) -stable. We can now take the largest such σ_γ to define persistence.

Definition 3.2. Let $\mathcal{C} : X \rightarrow L$ be a classifier, $x \in X$, and $\gamma \in (0, 1)$. Let σ_γ^* be the maximum σ_γ such that x is (γ, σ) -stable with respect to \mathcal{C} for all $\sigma < \sigma_\gamma$. We say that x has γ -persistence σ_γ^* .

The γ -persistence quantity σ_γ^* measures the stability of the neighborhood of a given x with respect to the output classification. Small persistence indicates that the classifier is unstable in a small neighborhood of x , whereas large persistence indicates stability of the classifier in a small neighborhood of x . In the later experiments, we have generally taken $\gamma = 0.7$. This choice is arbitrary and chosen to fit the problems considered here. In our experiments, we did not see significant change in results with small changes in the choice of γ , see Appendix Figure 16.

In our experiments, we numerically estimate γ -persistence via a bisection algorithm that we term the Bracketing Algorithm. Briefly, the algorithm first chooses search space bounds σ_{\min} and σ_{\max} such that x is (γ, σ_{\min}) -stable but is not (γ, σ_{\max}) -stable with respect to \mathcal{C} , and then proceeds to evaluate stability by bisection until an approximation of σ_γ^* is obtained.

Another natural approach would be to compute and sample a distribution tailored for the geometry around our chosen point instead of a gaussian. This could be done using non-parametric estimation or by performing an iterative computation of eigenvalues and eigenvectors. In this case, we could use a selection of eigenvalues to provide different $\sigma_{\gamma,i}$ for each eigenvector corresponding to the modes of variation in the distribution. It may be possible to use a tangent kernel approximation of a neural network like that proposed in [3] to compute these modes of variation directly from model parameters. We believe that this approach will likely perform well in further mapping geometric properties of neural networks, although we will show that our persistence metric performs well despite lacking this more structured information.

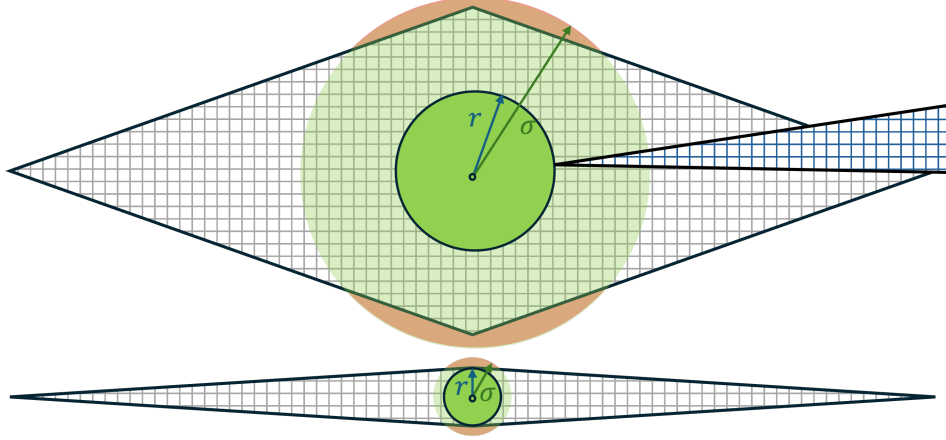


Figure 1: Both hard (middle) and soft (transparent outer) balls conform to the most constricted geometric region (bottom). However, the hard ball is also sensitive to rare counter-examples (above spike). By working with a soft ball, we need only compute a likelihood rather than an exhaustive search for rare examples. In addition, the soft-ball still responds correctly to macro-scale geometric features.

3.2 Decision Boundaries

In order to examine decision boundaries and their properties, we will carefully define the decision boundary in a variety of equivalent formulations.

3.2.1 The Argmax Function Arises in Multi-Class Problems

A central issue when writing classifiers is mapping from continuous outputs or probabilities as shown in 2 to discrete sets of classes. Frequently argmax type functions are used to accomplish this mapping. To discuss decision boundaries, we must precisely define argmax and some of its properties.

In practice, argmax is not strictly a function, but rather a mapping from the set of outputs or activations from another model into the power set of a discrete set of classes:

$$\text{argmax} : \mathbb{R}^k \rightarrow \mathcal{P}(L) \quad (2)$$

Defined this way, we cannot necessarily consider argmax to be a function in general as the singleton outputs of argmax overlap in an undefined way with other sets from the power set. However, if we restrict our domain carefully, we can identify certain properties. Restricting to only the pre-image of the singletons, it should be clear that argmax is constant. Indeed, restricted to the pre-image of any set in the power-set, argmax is constant and thus continuous. This induces the discrete topology whereby the pre-image of an individual singleton is open. Observe that for any point whose image is a singleton, one element of the domain vector must exceed the others by $\varepsilon > 0$. We shall use the ℓ^1 metric for distance, and thus if we restrict ourselves to a ball of radius ε , then all elements inside this ball will have that element still larger than the rest and thus map to the same singleton under argmax. Since the union of infinitely many open sets is open in \mathbb{R}^k , the union of all singleton pre-images is an open set. Conveniently this also provides proof that the union of all of the non-singleton sets in $\mathcal{P}(C)$ is a closed set. We will call this closed set the argmax Decision Boundary. We will list two equivalent formulations for this boundary.

Complement Definition A point x is in the *decision interior* D'_C for a classifier $C : \mathbb{R}^N \rightarrow L$ if there exists $\delta > 0$ such that $\forall \epsilon < \delta$, the number of elements $n(C(B_\epsilon(x))) = 1$.

The *decision boundary* of a classifier C is the closure of the complement of the decision interior $\overline{\{x : x \notin D'_C\}}$.

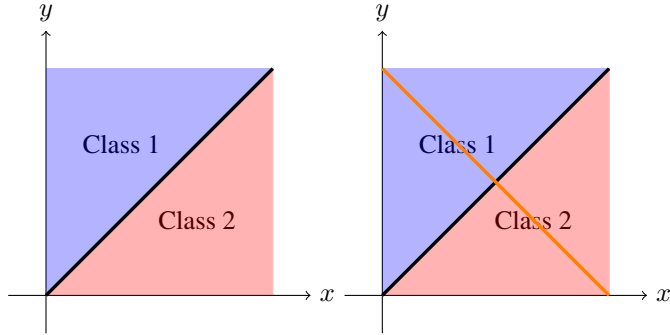


Figure 2: Decision boundary in $[0, 1] \times [0, 1]$ (left) and decision boundary restricted to probabilities (right). If the output of F are *probabilities* which add to one, then all points of x will map to the orange line (right). We note that the point $(0.5, 0.5)$ is therefore the only point on the decision boundary for probability valued F . We may generalize to higher dimensions where all probability valued models F will map into the the plane $x + y + z + \dots = 1$ in Y and the decision boundary will be partitioned into $K - 1$ components, where the K -decision boundary is the intersection of this plane with the *centroid* line $x = y = z = \dots$ and the 2-decision boundaries become planes intersecting at the same line.

Level Set Definition For an input space X , the decision boundary $D \subset X$ of a probability valued function f is the pre-image of a union of all level sets of outputs $f(X) = c_1, c_2, \dots, c_k$ defined by a constant c such that for some set of indices I , we have $c = c_i$ for every i in I and $c > c_j$ for every j not in I . The pre-image of each such set are all x such that $f(x) = A_c$ for some c .

4 Experiments

In this section we investigate the stability and persistence behavior of natural and adversarial examples for MNIST [32] and ImageNet [45] using a variety of different classifiers. For each set of image samples generated for a particular dataset, model, and attack protocol, we study (γ, σ) -stability and γ -persistence of both natural and adversarial images, and also compute persistence along trajectories from natural to adversarial images. In general, we use $\gamma = 0.7$ as a balance of being large enough that it is always possible to pick a σ that yields a set of samples whose fraction of the original class is meaningfully less than γ , and small enough that σ is likely to converge to a relatively precise number. While observed behavior near decision boundaries does not change much for small changes in γ (e.g. 0.7 vs 0.8 vs 0.9, see Appendix Figure 16), we note that as γ approaches 1, the number of samples needed to compute σ with precision rises asymptotically since the likelihood of finding sufficient samples not in the original class goes to zero. While most of the adversarial attacks considered here have a clear target class, the measurement of persistence does not require considering a particular candidate class. Furthermore, we will evaluate decision boundary incidence angles and apply our conclusions to evaluate models trained with manifold aligned gradients.

4.1 MNIST Experiments

Since MNIST is relatively small compared to ImageNet, we trained several classifiers with various architectures and complexities and implemented the adversarial attacks directly. Adversarial examples were generated against each of these models using Iterative Gradient Sign Method (IGSM [30]) and Limited-memory Broyden-Fletcher-Goldfarb-Shanno (L-BFGS [36]).

4.1.1 Investigation of (γ, σ) -stability on MNIST

We begin with a fully connected ReLU network with layers of size 784, 100, 20, and 10 and small regularization $\lambda = 10^{-7}$ which is trained on the standard MNIST [32] training set. We then start with a randomly selected MNIST test image x_1 from the 1's class and generate adversarial examples x_0, x_2, \dots, x_9 using IGSM for each target class other than 1. The neighborhoods around each x_i are examined by generating 1000 i.i.d. samples from $N(x_i, \sigma^2 I)$ for each of 100 equally spaced

standard deviations $\sigma \in (0, 1.6)$. Figure 3 shows the results of the Gaussian perturbations of a natural example x_1 of the class labeled 1 and the results of Gaussian perturbations of the adversarial example x_0 targeted at the class labeled 0. We provide other examples of x_2, \dots, x_9 in the supplementary materials. Note that the original image is very stable under perturbation, while the adversarial image is not.

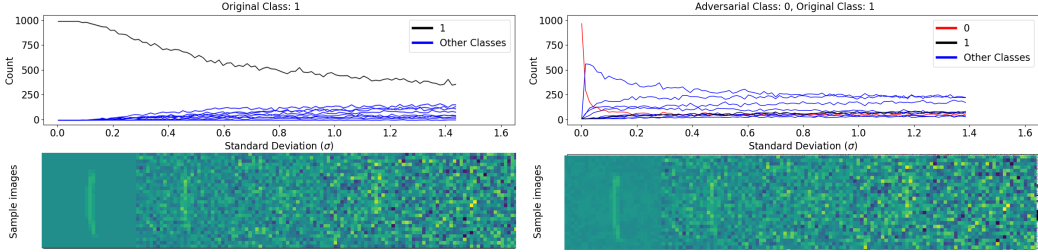


Figure 3: Frequency of each class in Gaussian samples with increasing variance around a natural image of class 1 (left) and around an adversarial attack of that image targeted at 0 generated using IGSM (right). The adversarial class (0) is shown as a red curve. The natural image class (1) is shown in black. Bottoms show example sample images at different standard deviations for natural (left) and adversarial (right) examples.

4.1.2 Persistence of adversarial examples for MNIST

To study persistence of adversarial examples on MNIST, we take the same network architecture as in the previous subsection and randomly select 200 MNIST images. For each image, we used IGSM to generate 9 adversarial examples (one for each target class) yielding a total of 1800 adversarial examples. In addition, we randomly sampled 1800 natural MNIST images. For each of the 3600 images, we computed 0.7-persistence; the results are shown in Figure 4. One sees that 0.7-persistence of adversarial examples tends to be significantly smaller than that of natural examples for this classifier, indicating that they are generally less stable than natural images. We will see subsequently that this behavior is typical.

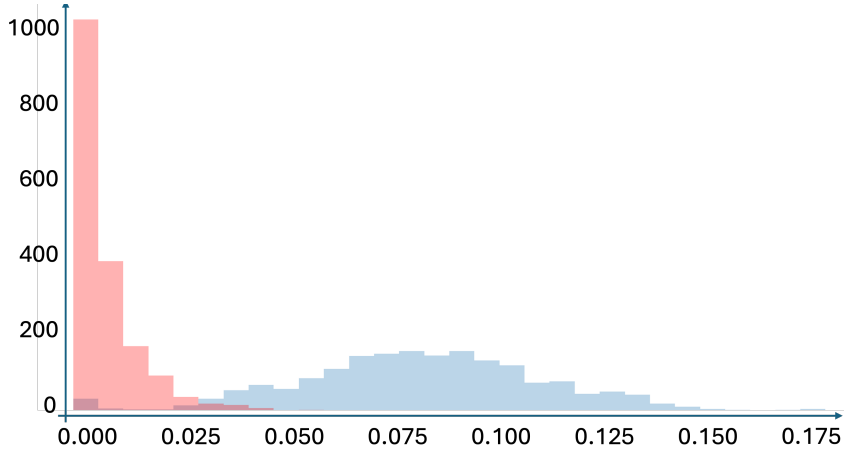


Figure 4: Histogram of 0.7-persistence of IGSM-based adversarial examples (red) and natural examples (blue) on MNIST.

Next, we investigate the relationship of network complexity and (γ, σ) -stability by revisiting the now classic work of Szegedy et al. [52] on adversarial examples.

Table 1 recreates and adds on to part of [52, Table 1] in which networks of differing complexity are trained and attacked using L-BFGS. The table contains new columns showing the average 0.7-persistence for both natural and adversarial examples for each network, as well as the average distortion for the adversarial examples. The distortion is the ℓ^2 -norm divided by square root of

the dimension n . The first networks listed are of the form FC10-k, and are fully connected single layer ReLU networks that map each input vector $x \in \mathbb{R}^{784}$ to an output vector $y \in \mathbb{R}^{10}$ with a regularization added to the objective function of the form $\lambda \|w\|_2 / N$, where $\lambda = 10^{-k}$ and N is the number of parameters in the weight vector w defining the network. The higher values of λ indicate more regularization.

FC100-100-10 and FC200-200-10 are networks with 2 hidden layers (with 100 and 200 nodes, respectively) with regularization added for each layer and λ for each layer equal to 10^{-5} , 10^{-5} , and 10^{-6} . Training for these networks was conducted with a fixed number of epochs (typically 21). For the bottom half of Table 1, we also considered networks with four convolutional layers plus a max-pooling layer connected by ReLU to a fully connected hidden layer with increasing numbers of channels denoted as “C-Ch,” where C reflects that this is a CNN and Ch denotes the number of channels. A more detailed description of these networks can be found in Appendix B.

Table 1: Recreation of Szegedy et al. [52, Table 1] for the MNIST dataset. For each network, we show Testing Accuracy (in %), Average Distortion ($\|x\|_2 / \sqrt{n}$) of adversarial examples, and new columns show average 0.7-persistence values for natural (Nat) and adversarial (Adv) images. 300 natural and 300 adversarial examples generated with L-BFGS were used for each aggregation.

Network	Test Acc	Avg Dist	Persist (Nat)	Persist (Adv)
FC10-4	92.09	0.123	0.93	1.68
FC10-2	90.77	0.178	1.37	4.25
FC10-0	86.89	0.278	1.92	12.22
FC100-100-10	97.31	0.086	0.65	0.56
FC200-200-10	97.61	0.087	0.73	0.56
C-2	95.94	0.09	3.33	0.027
C-4	97.36	0.12	0.35	0.027
C-8	98.50	0.11	0.43	0.0517
C-16	98.90	0.11	0.53	0.0994
C-32	98.96	0.11	0.78	0.0836
C-64	99.00	0.10	0.81	0.0865
C-128	99.17	0.11	0.77	0.0883
C-256	99.09	0.11	0.83	0.0900
C-512	99.22	0.10	0.793	0.0929

The main observation from Table 1 is that for higher complexity networks, adversarial examples tend to have smaller persistence than natural examples. Histograms reflecting these observations can be found in the supplemental material. Another notable takeaway is that for models with fewer effective parameters, the attack distortion necessary to generate a successful attack is so great that the resulting image is often more stable than a natural image under that model, as seen particularly in the FC10 networks. Once there are sufficiently many parameters available in the neural network, we found that both the average distortion of the adversarial examples and the average 0.7-persistence of the adversarial examples tended to be smaller. This observation is consistent with the idea that networks with more parameters are more likely to exhibit decision boundaries with more curvature.

4.2 Results on ImageNet

For ImageNet [11], we used pre-trained ImageNet classification models, including alexnet [28] and vgg16 [51].

We then generated attacks based on the ILSVRC 2015 [45] validation images for each of these networks using a variety of modern attack protocols, including Fast Gradient Sign Method (FGSM [17]), Momentum Iterative FGSM (MIFGSM [12]), Basic Iterative Method (BIM [30]), Projected Gradient Descent (PGD [38]), Randomized FGSM (R+FGSM [57]), and Carlini-Wagner (CW Carlini and Wagner [6]). These were all generated using the TorchAttacks by Kim [26] tool-set.

4.2.1 Investigation of (γ, σ) -stability on ImageNet

In this section, we show the results of Gaussian neighborhood sampling in ImageNet. Figures 5 and 6 arise from vgg16 and adversarial examples created with BIM; results for other networks and attack strategies are similar, with additional figures in the supplementary material. Figure 5 (left) begins with an image x with label `goldfinch`. For each equally spaced $\sigma \in (0, 2)$, 100 i.i.d. samples were drawn from the Gaussian distribution $N(x, \sigma^2 I)$, and the counts of the vgg16 classification for each label are shown. In Figure 5 (right), we see the same plot, but for an adversarial example targeted at the class `indigo_bunting`, which is another type of bird, using the BIM attack protocol.

The key observation in Figure 5 is that the frequency of the class of the adversarial example (`indigo_bunting`, shown in red) falls off much quicker than the class for the natural example (`goldfinch`, shown in black). In this particular example, the original class appears again after the adversarial class becomes less prevalent, but only for a short period of σ , after which other classes begin to dominate. In some examples the original class does not dominate at all after the decline of the adversarial class. The adversarial class almost never dominates for a long period of σ .

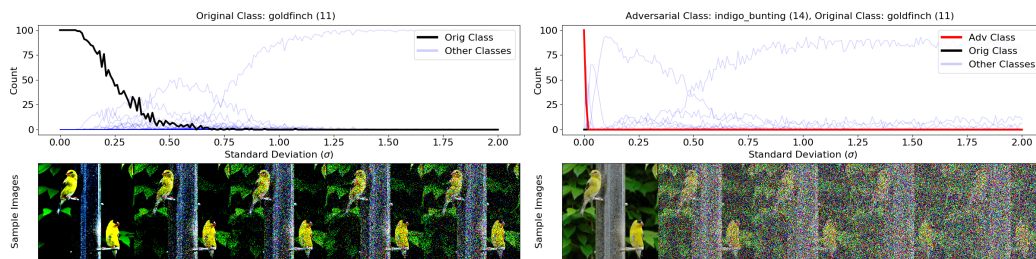


Figure 5: Frequency of each class in Gaussian samples with increasing variance around a `goldfinch` image (left) and an adversarial example of that image targeted at the `indigo_bunting` class and calculated using the BIM attack (right). Bottoms show example sample images at different standard deviations for natural (left) and adversarial (right) examples.

4.2.2 Persistence of adversarial examples on ImageNet

Figure 6 shows a plot of the 0.7-persistence along the straight-line path between a natural example and adversarial example as parameterized between 0 and 1. It can be seen that the drop off of persistence occurs precisely around the decision boundary. This indicates some sort of curvature favoring the class of the natural example, since otherwise the persistence would be roughly the same as the decision boundary is crossed.

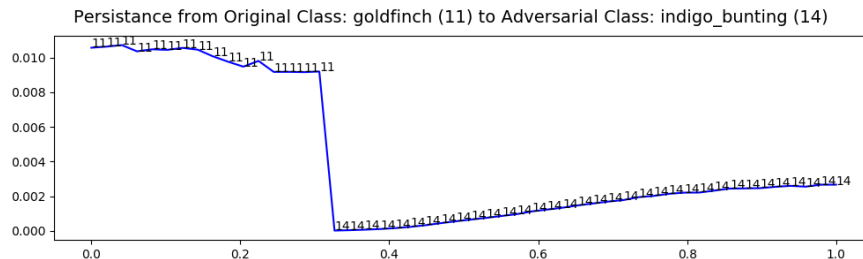


Figure 6: The 0.7-persistence of images along the straight line path from an image in class `goldfinch` (11) to an adversarial image generated with BIM in the class `indigo_bunting` (14) on a vgg16 classifier. The classification of each image on the straight line is listed as a number so that it is possible to see the transition from one class to another. The vertical axis is 0.7-persistence and the horizontal axis is progress towards the adversarial image.

An aggregation of persistence for many randomly selected images from the `goldfinch` class in the validation set for Imagenet are presented in Table 2. For each image of a `goldfinch` and for each network of alexnet and vgg16, attacks were prepared to a variety of 28 randomly selected

Network/Method	Avg Dist	Persist (Nat)	Persist (Adv)
alexnet (total)	0.0194	0.0155	0.0049
BIM	0.0188	0.0162	0.0050
MIFGSM	0.0240	0.0159	0.0053
PGD	0.0188	0.0162	0.0050
vgg16 (total)	0.0154	0.0146	0.0011
BIM	0.0181	0.0145	0.0012
MIFGSM	0.0238	0.0149	0.0018
PGD	0.0181	0.0145	0.0012

Table 2: The 0.7-persistence values for natural (Nat) and adversarial (Adv) images along with average distortion for adversarial images of alexnet and vgg16 for attacks generated with BIM, MIFGSM, and PGD on images from class `goldfinch` targeted toward other classes from the ILSVRC 2015 classification labels.

targets using a BIM, MIFGSM, PGD, FGSM, R+FGSM, and CW attack strategies. The successful attacks were aggregated and their 0.7-persistences were computed using the Bracketing Algorithm along with the 0.7-persistences of the original images from which each attack was generated. Each attack strategy had a slightly different mixture of which source image and attack target combinations resulted in successful attacks. The overall rates for each are listed, as well as particular results on the most successful attack strategies in our experiments, BIM, MIFGSM, and PGD. The results indicate that adversarial images generated for these networks (alexnet and vgg16) using these attacks were less persistent, and hence less stable, than natural images for the same models.

4.3 Decision Boundary Interpolation and Angle Measurement

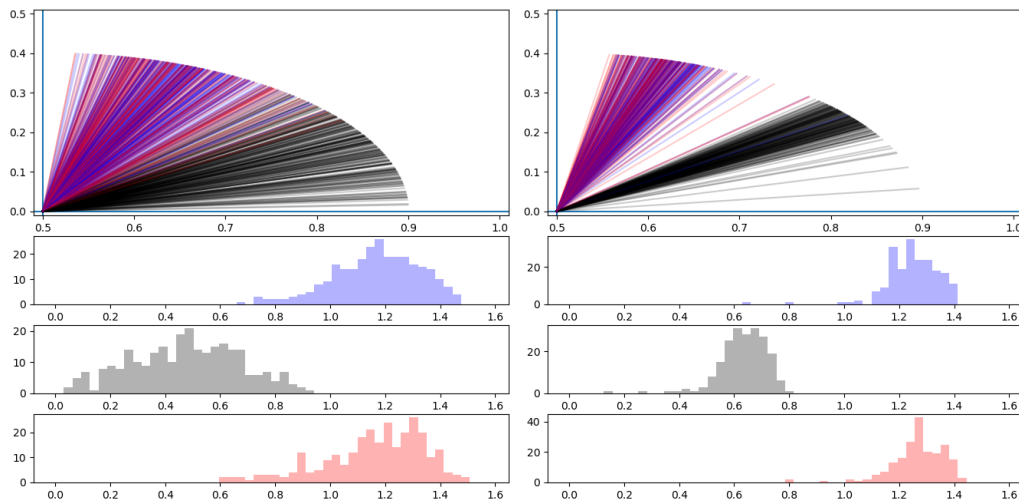


Figure 7: Decision boundary incident angles between test to test interpolation and a computed normal vector to the decision boundary images (left) and between test and adversarial images (right). Angles (plotted Top) are referenced to decision boundary so $\pi/2$ radians (right limit of plots) corresponds with perfect orthogonality to decision boundary. Lines and histograms measure angles of training gradients (Top) linear interpolant (Middle) and adversarial gradients (Bottom). x and y axes are the axes of the unit-circle so angles can be compared. All angles are plotted in the upper-right quadrant for brevity. The lower plots are all histograms with their y axes noting counts and their x -axes showing angles all projected to the range from 0 to $\pi/2$.

In order to understand this sudden drop in persistence across the decision boundary observed in Figure 6, we will investigate incident angle of the interpolation with the decision boundary. In order to measure these angles, we must first interpolate along the decision boundary between two points. We will do this for pairs of test and test and pairs of test and adversary. In both cases, we will

use a bracketing algorithm along the interpolation from candidate points to identify a point within machine-precision of the decision boundary x_b .

Next, we will take 5000 samples from a Gaussian centered at this point with small standard deviation $\sigma = 10^{-6}$. Next, for each sample, we will perform an adversarial attack in order to produce a corresponding point on the opposite side of the decision boundary. Now for this new pair (sample and attacked sample), we will repeat the interpolation bracketing procedure in order to obtain the projection of this sample onto the decision boundary along the attack trajectory. Next, we will use singular value decomposition (SVD) on the differences between the projected samples and our decision boundary point x_b to compute singular values and vectors from these projected samples. We will use the right singular vector corresponding with the smallest singular value as an approximation of a normal vector to the decision boundary at x_b . This point is difficult to compute due to degeneracy of SVD for small singular values, however in our tests, this value could be computed to a precision of 0.003. We will see that this level of precision exceeds that needed for the angles computed with respect to this normal vector sufficiently.

From Figure 7 we notice that neither training gradients nor adversarial gradients are orthogonal to the decision boundary. From a theory perspective, this is possible because this problem has more than 2 classes, so that the decision boundary includes $(0.34, 0.34, 0.32)$ and $(0.4, 0.4, 0.2)$. That is to say that the level set definition of the decision boundary has degrees of freedom that do not require orthogonality of gradients. More interestingly, both natural and adversarial linear interpolants tend to cross at acute angles with respect to the decision boundary, with adversarial attacks tending to be closer to orthogonal. This suggests that obliqueness of the decision boundary with respect to test points may be related to adversarial vulnerability. We will leverage this understanding with manifold alignment to see if constraining gradients to a lower dimensional manifold, and thus increasing orthogonality of gradients will increase robustness.

4.4 Manifold Alignment on MNIST via PCA

In order to provide an empirical measure of alignment, we first require a well defined image manifold. The task of discovering the true structure of k -dimensional manifolds in \mathbb{R}^d given a set of points sampled on the manifold has been studied previously [25]. Many algorithms produce solutions which are provably accurate under data density constraints. Unfortunately, these algorithms have difficulty extending to domains with large d due to the curse of dimensionality. Our solution to this fundamental problem is to sidestep it entirely by redefining our dataset. We begin by projecting our data onto a well known low dimensional manifold, which we can then measure with certainty.

We first fit a PCA model on all training data, using k components for each class to form a component matrix W , where $k \ll d$. Given the original dataset X , we create a new dataset $X_{\mathcal{M}} := \{x \times \mathbf{W}^T \times \mathbf{W} : x \in X\}$. We will refer to this set of component vectors as \mathbf{W} . Because the rank of the linear transformation matrix, k , is defined lower than the dimension of the input space, d , this creates a dataset which lies on a linear subspace of \mathbb{R}^d . This subspace is defined by the span of $X \times \mathbf{W}^T$ and any vector in \mathbb{R}^d can be projected onto it. Any data point drawn from $\{z \times \mathbf{W}^T : z \in \mathbb{R}^k\}$ is considered a valid datapoint. This gives us a continuous linear subspace which can be used as a data manifold.

Given that it is our goal to study the simplest possible case, we chose MNIST as the dataset to be projected and selected $k = 28$ components. We refer to this new dataset as Projected MNIST (PMNIST). The true rank of PMNIST is lower than that of the original MNIST data, meaning there was information lost in this projection. The remaining information we found is sufficient to achieve 92% accuracy using a baseline Multi-layer Perceptron (MLP), and the resulting images retain their semantic properties as shown in Figure 8.

4.5 Manifold Aligned Gradients

Component vectors extracted from the original dataset are used to project gradient examples onto our pre-defined image manifold.

Given a gradient example $\nabla_x = \frac{\partial f_{\theta}(x,y)}{\partial x}$ where f_{θ} represents a neural network parameterized by weights θ , ∇_x is transformed using the coefficient vectors \mathbf{W} .

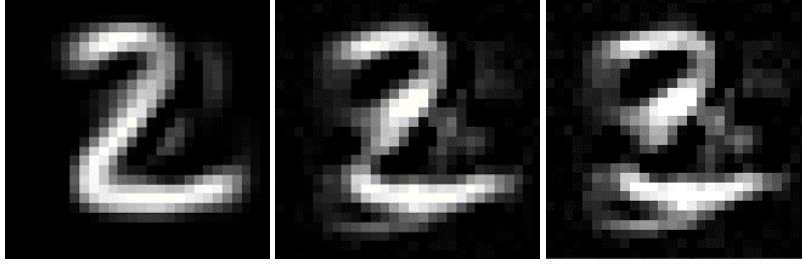


Figure 8: Visual example of manifold optimized model transforming 2 into 3. Original PMNIST image on left, center image is center point between original and attacked, on right is the attacked image. Transformation performed using PGD using the l_∞ norm. Visual evidence of manifold alignment is often subjective and difficult to quantify. This example is provided as a baseline to substantiate our claim that our empirical measurements of alignment are valid.

$$\rho_x = \nabla_x \times \mathbf{W}^T \times \mathbf{W} \quad (3)$$

The projection of the original vector onto this new transformed vector will be referred to as $P_{\mathcal{M}}$.

$$P_{\mathcal{M}}(\nabla_x) = \frac{\nabla_x \cdot \rho_x}{\|\rho_x\|_2} \cdot \frac{\rho_x}{\|\rho_x\|_2} \quad (4)$$

The ratio of norms of this projection gives a metric of manifold alignment.

$$\frac{\|\nabla_x\|}{\|P_{\mathcal{M}}(\nabla_x)\|} \quad (5)$$

This gives us a way of measuring the ratio between on-manifold and off-manifold components of the gradient. In addition to this loss formula, both cosine similarity and the vector rejection length were tested, but the norm ratio we found to be the most stable in training. We hypothesize that this is due to these other metrics becoming less convex, and thus less stable, when far from minima. It is unknown whether this result is true in general or if the specific dataset and optimization strategy used influenced which loss was most stable. We use this measure as both a metric and a loss, allowing us to optimize the following objective.

$$\mathbb{E}_{(x,y) \sim \mathcal{D}} \left[L(\theta, x, y) + \alpha \frac{\|\nabla_x\|}{\|P_{\mathcal{M}}(\nabla_x)\|} \right] \quad (6)$$

Where $L(\theta, x, y)$ represents our classification loss term and α is a hyper parameter determining the weight of the manifold loss term.

4.6 Manifold Alignment Robustness Results

All models were two layer MLPs with 1568 nodes in each hidden layer. The hidden layer size was chosen as twice the input size. This arrangement was chosen to maintain the simplest possible case.

Two types of attacks were leveraged in this study: fast gradient sign method (FGSM) [17] which performs a single step based on the sign of an adversarial gradient for each input and projected gradient descent (PGD) which performs gradient descent on input data using adversarial gradients in order to produce adversarial attacks [38]. A total of four models were trained and evaluated on these attacks: Baseline, Robust, Manifold and Manifold Robust. All models, including the baseline, were trained on PMNIST (a fixed permutation is applied to the training and test images of the MNIST dataset). ‘‘Robust’’ in our case refers to models trained with new adversarial examples labeled for their class *before* perturbation during each epoch consistent with Tramer and Boneh [55]. All robust models were trained using the l_∞ norm and a maximum perturbation parameter of $\epsilon = 0.1$. Manifold Robust refers to both optimizing our manifold objective and robust training simultaneously.

Figure 9 shows the cosine similarity of the gradient and its projection onto the reduced space W on the testing set of PMNIST for both the Manifold model and Robust model. Higher values (closer to 1) indicate the model is more aligned with the manifold. Both robust and MAG models here are

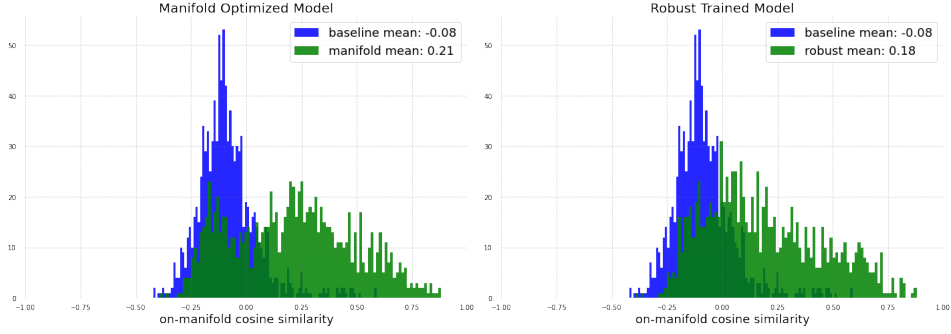


Figure 9: Comparison of on-manifold components between baseline network, robust trained models, and manifold optimized models. Large values indicate higher similarity to the manifold. Y -axes for both plots are histogram counts. Both robust and manifold optimized models are more 'on-manifold' than the baseline, with adversarial training being slightly less so.

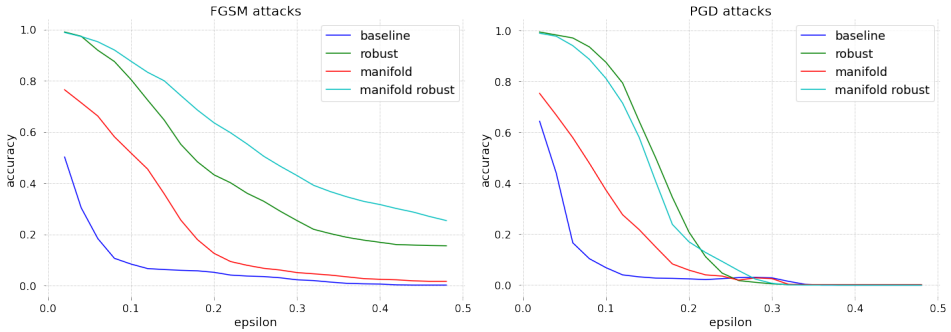


Figure 10: Comparison of adversarial robustness for PMNIST models under various training conditions. Attacks are prepared using a range of a distortion parameter epsilon. For FGSM, the sign of the gradient is multiplied by each epsilon. For PGD, epsilon is determined by a weight on the l_2 norm term of the adversarial loss function. Many variations of the l_2 weight are performed, and then they are aggregated and the distance of each perturbation is plotted as epsilon. For both FGSM and PGD, we see a slight increase in robustness from using manifold optimization. Adversarial training still improves performance significantly more than manifold optimization. Another observation to note is that when both the manifold, and adversarial objective were optimized, increased robustness against FGSM attacks was observed. All robust models were trained using the l_∞ norm at epsilon = 0.1.

shown to be more on manifold than the Baseline. This demonstrates that our metric for alignment is being optimized as a consequence of adversarial training.

Figure 10 shows the adversarial robustness of each model. In both cases, aligning the model to the manifold shows an increase in accuracy of classification for adversarial images over the baseline. However, we do not consider the performance boost against PGD to be significant enough to call these models robust against PGD attacks. Another point of interest that while using both our manifold alignment metric and adversarial training, we see an even greater improvement against FGSM attacks.

The fact that this performance increase is not shared by PGD training may indicate a relationship between these methods. Our current hypothesis is that a linear representation of the image manifold is sufficient to defend against linear attacks such as FGSM, but cannot defend against a non-linear adversary.

5 Conclusion

In order to better understand the observed tendency for points near natural data to be classified similarly and points near adversarial examples to be classified differently, we defined a notion of (γ, σ) -stability which is easily estimated by Monte Carlo sampling. For any data point x , we then

define the γ -persistence to be the smallest σ_γ such that the probability of similarly classified data is at least γ when sampling from Gaussian distributions with mean x and standard deviation less than σ_γ . The persistence value can be quickly estimated by a Bracketing Algorithm. These two measures were considered with regard to both the MNIST and ImageNet datasets and with respect to a variety of classifiers and adversarial attacks. We found that adversarial examples were much less stable than natural examples in that the 0.7-persistence for natural data was usually significantly larger than the 0.7-persistence for adversarial examples. We also saw that the dropoff of the persistence tends to happen precisely near the decision boundary. Each of these observations is strong evidence toward the hypothesis that adversarial examples arise inside cones or high curvature regions in the adversarial class, whereas natural images lie outside such regions.

We also found that often the most likely class for perturbations of an adversarial examples is a class other than the class of the original natural example used to generate the adversarial example; instead, some other background class is favored. In addition, we found that some adversarial examples may be more stable than others, and a more detailed probing using the concept of (γ, σ) -stability and the γ -persistence statistic may be able to help with a more nuanced understanding of the geometry and curvature of the decision boundary. Although not pursued here, the observations and statistics used in this paper could potentially be used to develop methods to detect adversarial examples as in [10, 14, 19, 34, 43, 44] and others. As with other methods of detection, this may be susceptible to adaptive attacks as discussed by Tramèr et al. [56]. Critically, our results summarized in Table 1 indicate that for more regularized and smaller models, model accuracy is not necessarily a good indicator of resistance to adversarial attacks. We believe that measurement of distortion and even a metric like persistence should be a core part of adversarial robustness evaluation augmenting standard practice as set forward by Carlini et al. [7].

For the future, we have made several observations: We found that some adversarial examples may be more stable than others. More detailed probing using the concept of (γ, σ) -stability and the γ -persistence along linear interpolation between natural images and between natural and adversarial images reveals sharp drops in persistence. Sharp drops in persistence correspond with oblique angles of incidence between linear interpolation vectors and the decision boundary learned by neural networks. Combining these observations, we can form a conjecture: Adversarial examples appear to exist near regions surrounded by negatively curved structures bounded by decision surfaces with relatively small angles relative to linear interpolation among training and testing data. This conjecture compares with the dimpled manifold hypothesis [50], however our techniques provide geometric information that allows us to gain a more detailed analysis of this region than in that work. In addition, our analysis of gradient alignment with manifolds reinforces the notion that the obliqueness we observe may be a property which can be isolated and trained out of neural networks to some extent. Future work should focus on refining this conjecture with further tools to complete the spatial and mathematical picture surrounding adversarial examples.

Acknowledgments and Disclosure of Funding

This material is based upon work supported by the Department of Energy (National Nuclear Security Administration Minority Serving Institution Partnership Program’s CONNECT - the Consortium on Nuclear sECurity Technologies) DE-NA0004107. This report was prepared as an account of work sponsored by an agency of the United States Government. Neither the United States Government nor any agency thereof, nor any of their employees, makes any warranty, express or implied, or assumes any legal liability or responsibility for the accuracy, completeness, or usefulness of any information, apparatus, product, or process disclosed, or represents that its use would not infringe privately owned rights. The views and opinions of authors expressed herein do not necessarily state or reflect those of the United States Government or any agency thereof.

We would like to acknowledge funding from NSF TRIPODS Award Number 1740858 and NSF RTG Applied Mathematics and Statistics for Data-Driven Discovery Award Number 1937229. The manifold alignment portion of this research was supported by LANL’s Laboratory Directed Research and Development (LDRD) program under project number 20210043DR.

References

- [1] J. Adebayo, J. Gilmer, M. Muelly, I. Goodfellow, M. Hardt, and B. Kim. Sanity checks for saliency maps. *Advances in neural information processing systems*, 31, 2018.
- [2] G. Aparne, A. Banburski, and T. Poggio. Pca as a defense against some adversaries. Technical report, Center for Brains, Minds and Machines (CBMM), 2022.
- [3] B. Bell, M. Geyer, D. Glickenstein, A. S. Fernandez, and J. Moore. An exact kernel equivalence for finite classification models. *CoRR*, abs/2308.00824, 2023. doi: 10.48550/arXiv.2308.00824. URL <https://doi.org/10.48550/arXiv.2308.00824>.
- [4] T. Blau, R. Ganz, C. Baskin, M. Elad, and A. M. Bronstein. Classifier robustness enhancement via test-time transformation. *CoRR*, abs/2303.15409, 2023. doi: 10.48550/ARXIV.2303.15409. URL <https://doi.org/10.48550/arXiv.2303.15409>.
- [5] A. Blum, T. Dick, N. Manoj, and H. Zhang. Random smoothing might be unable to certify l^∞ robustness for high-dimensional images. *The Journal of Machine Learning Research*, 21(1): 8726–8746, 2020.
- [6] N. Carlini and D. Wagner. Towards evaluating the robustness of neural networks. *arXiv:1608.04644 [cs]*, Aug. 2016. URL <http://arxiv.org/abs/1608.04644>. arXiv: 1608.04644.
- [7] N. Carlini, A. Athalye, N. Papernot, W. Brendel, J. Rauber, D. Tsipras, I. J. Goodfellow, A. Madry, and A. Kurakin. On evaluating adversarial robustness. *CoRR*, abs/1902.06705, 2019. URL <http://arxiv.org/abs/1902.06705>.
- [8] C. Chen, J. Zhang, X. Xu, L. Lyu, C. Chen, T. Hu, and G. Chen. Decision boundary-aware data augmentation for adversarial training. *IEEE Transactions on Dependable and Secure Computing*, 20(3):1882–1894, 2023. doi: 10.1109/TDSC.2022.3165889.
- [9] J. Cohen, E. Rosenfeld, and Z. Kolter. Certified adversarial robustness via randomized smoothing. In *international conference on machine learning*, pages 1310–1320. PMLR, 2019.
- [10] F. Crecchi, D. Bacciu, and B. Biggio. Detecting adversarial examples through nonlinear dimensionality reduction. In *27th European Symposium on Artificial Neural Networks, Computational Intelligence and Machine Learning - ESANN '19*, pages 483–488, 2019.
- [11] J. Deng, W. Dong, R. Socher, L.-J. Li, K. Li, and L. Fei-Fei. Imagenet: A large-scale hierarchical image database. In *2009 IEEE conference on computer vision and pattern recognition*, pages 248–255. IEEE, 2009.
- [12] Y. Dong, F. Liao, T. Pang, H. Su, J. Zhu, X. Hu, and J. Li. Boosting adversarial attacks with momentum. In *2018 IEEE Conference on Computer Vision and Pattern Recognition, (CVPR) 2018, Salt Lake City, UT, USA, June 18-22, 2018*, pages 9185–9193.
- [13] A. Fawzi, S.-M. Moosavi-Dezfooli, P. Frossard, and S. Soatto. Empirical study of the topology and geometry of deep networks. In *Proceedings of the IEEE Conference on Computer Vision and Pattern Recognition (CVPR)*, June 2018.
- [14] N. Frosst, S. Sabour, and G. E. Hinton. DARCCC: detecting adversaries by reconstruction from class conditional capsules. *CoRR*, abs/1811.06969, 2018. URL <http://arxiv.org/abs/1811.06969>.
- [15] R. Ganz, B. Kawar, and M. Elad. Do perceptually aligned gradients imply adversarial robustness? *arXiv preprint arXiv:2207.11378*, 2022.
- [16] J. Gilmer, L. Metz, F. Faghri, S. S. Schoenholz, M. Raghu, M. Wattenberg, and I. J. Goodfellow. Adversarial spheres. In *6th International Conference on Learning Representations, (ICLR 2018), Vancouver, BC, Canada*.
- [17] I. J. Goodfellow, J. Shlens, and C. Szegedy. Explaining and harnessing adversarial examples. In Y. Bengio and Y. LeCun, editors, *3rd International Conference on Learning Representations, ICLR 2015, San Diego, CA, USA*.

- [18] W. He, B. Li, and D. Song. Decision boundary analysis of adversarial examples. In *International Conference on Learning Representations*, 2018. URL <https://openreview.net/forum?id=BkpiPMbA->.
- [19] H. Hosseini, S. Kannan, and R. Poovendran. Are odds really odd? bypassing statistical detection of adversarial examples. *CoRR*, abs/1907.12138, 2019. URL <http://arxiv.org/abs/1907.12138>.
- [20] S. Hu, T. Yu, C. Guo, W. Chao, and K. Q. Weinberger. A new defense against adversarial images: Turning a weakness into a strength. In H. M. Wallach, H. Larochelle, A. Beygelzimer, F. d’Alché-Buc, E. B. Fox, and R. Garnett, editors, *Advances in Neural Information Processing Systems 32 (NeurIPS 2019) Vancouver, BC, Canada*, pages 1633–1644.
- [21] A. Ilyas, S. Santurkar, D. Tsipras, L. Engstrom, B. Tran, and A. Madry. Adversarial examples are not bugs, they are features. In H. M. Wallach, H. Larochelle, A. Beygelzimer, F. d’Alché-Buc, E. B. Fox, and R. Garnett, editors, *Advances in Neural Information Processing Systems 32 (NeurIPS 2019) Vancouver, BC, Canada*, pages 125–136, 2019.
- [22] H. Jin, J. Chen, H. Zheng, Z. Wang, J. Xiao, S. Yu, and Z. Ming. Roby: Evaluating the adversarial robustness of a deep model by its decision boundaries. *Information Sciences*, 587:97–122, 2022. ISSN 0020-0255. doi: <https://doi.org/10.1016/j.ins.2021.12.021>. URL <https://www.sciencedirect.com/science/article/pii/S0020025521012421>.
- [23] J. Jo and Y. Bengio. Measuring the tendency of cnns to learn surface statistical regularities. *arXiv preprint arXiv:1711.11561*, 2017.
- [24] S. Kaur, J. Cohen, and Z. C. Lipton. Are perceptually-aligned gradients a general property of robust classifiers? *arXiv preprint arXiv:1910.08640*, 2019.
- [25] M. Houry and D. Hadfield-Menell. On the geometry of adversarial examples. *CoRR*, abs/1811.00525, 2018.
- [26] H. Kim. Torchattacks : A pytorch repository for adversarial attacks. *CoRR*, abs/2010.01950, 2020.
- [27] P.-J. Kindermans, S. Hooker, J. Adebayo, M. Alber, K. T. Schütt, S. Dähne, D. Erhan, and B. Kim. The (un) reliability of saliency methods. In *Explainable AI: Interpreting, Explaining and Visualizing Deep Learning*, pages 267–280. Springer, 2019.
- [28] A. Krizhevsky, I. Sutskever, and G. E. Hinton. Imagenet classification with deep convolutional neural networks. In F. Pereira, C. J. C. Burges, L. Bottou, and K. Q. Weinberger, editors, *Advances in Neural Information Processing Systems*, volume 25, 2012.
- [29] A. Kumar, A. Levine, T. Goldstein, and S. Feizi. Curse of dimensionality on randomized smoothing for certifiable robustness. In *International Conference on Machine Learning*, pages 5458–5467. PMLR, 2020.
- [30] A. Kurakin, I. J. Goodfellow, and S. Bengio. Adversarial examples in the physical world. In *5th International Conference on Learning Representations, ICLR 2017, Toulon, France*.
- [31] P. Langley. Crafting papers on machine learning. In P. Langley, editor, *Proceedings of the 17th International Conference on Machine Learning (ICML 2000)*, pages 1207–1216, Stanford, CA, 2000. Morgan Kaufmann.
- [32] Y. LeCun and C. Cortes. MNIST handwritten digit database. 2010. URL <http://yann.lecun.com/exdb/mnist/>.
- [33] M. Lecuyer, V. Atlidakis, R. Geambasu, D. Hsu, and S. Jana. Certified robustness to adversarial examples with differential privacy. In *2019 IEEE Symposium on Security and Privacy (SP)*, pages 656–672. IEEE, 2019.
- [34] K. Lee, K. Lee, H. Lee, and J. Shin. A simple unified framework for detecting out-of-distribution samples and adversarial attacks. In *NeurIPS*, 2018.

- [35] B. Li, C. Chen, W. Wang, and L. Carin. Certified adversarial robustness with additive noise. *Advances in neural information processing systems*, 32, 2019.
- [36] D. C. Liu and J. Nocedal. On the limited memory BFGS method for large scale optimization. *Mathematical Programming*, 45(1-3):503–528, 1989.
- [37] Z. Lu, H. Hu, S. Huo, and S. Li. Mr2d: Multiple random masking reconstruction adversarial detector. In *2022 10th International Conference on Information Systems and Computing Technology (ISCTech)*, pages 61–67, 2022. doi: 10.1109/ISCTech58360.2022.00016.
- [38] A. Madry, A. Makelov, L. Schmidt, D. Tsipras, and A. Vladu. Towards deep learning models resistant to adversarial attacks. In *6th International Conference on Learning Representations, ICLR 2018, Vancouver, BC, Canada*.
- [39] G. Magai and A. Ayzenberg. Topology and geometry of data manifold in deep learning, 2022.
- [40] D. Nguyen Minh and A. T. Luu. Textual manifold-based defense against natural language adversarial examples. In *Proceedings of the 2022 Conference on Empirical Methods in Natural Language Processing*, pages 6612–6625, Abu Dhabi, United Arab Emirates, Dec. 2022. Association for Computational Linguistics. URL <https://aclanthology.org/2022.emnlp-main.443>.
- [41] G. Osada, T. Takahashi, B. Ahsan, and T. Nishide. Out-of-distribution detection with reconstruction error and typicality-based penalty. In *Proceedings of the IEEE/CVF Winter Conference on Applications of Computer Vision (WACV)*, pages 5551–5563, January 2023.
- [42] A. Prakash, N. Moran, S. Garber, A. DiLillo, and J. A. Storer. Deflecting adversarial attacks with pixel deflection. In *2018 IEEE Conference on Computer Vision and Pattern Recognition (CVPR) Salt Lake City, UT, USA*, pages 8571–8580.
- [43] Y. Qin, N. Frosst, S. Sabour, C. Raffel, G. W. Cottrell, and G. E. Hinton. Detecting and diagnosing adversarial images with class-conditional capsule reconstructions. In *8th International Conference on Learning Representations, (ICLR 2020), Addis Ababa, Ethiopia*.
- [44] K. Roth, Y. Kilcher, and T. Hofmann. The odds are odd: A statistical test for detecting adversarial examples. In K. Chaudhuri and R. Salakhutdinov, editors, *Proceedings of the 36th International Conference on Machine Learning (ICML)*, volume 97, pages 5498–5507, 2019.
- [45] O. Russakovsky, J. Deng, H. Su, J. Krause, S. Satheesh, S. Ma, Z. Huang, A. Karpathy, A. Khosla, M. Bernstein, A. C. Berg, and L. Fei-Fei. ImageNet Large Scale Visual Recognition Challenge. *International Journal of Computer Vision (IJCV)*, 115(3):211–252, 2015. doi: 10.1007/s11263-015-0816-y.
- [46] J. Schmidhuber. Deep learning in neural networks: An overview. *Neural Networks*, 61:85 – 117, 2015.
- [47] A. Shafahi, W. R. Huang, C. Studer, S. Feizi, and T. Goldstein. Are adversarial examples inevitable? In *International Conference on Learning Representations (ICLR)*, 2019.
- [48] H. Shah, P. Jain, and P. Netrapalli. Do input gradients highlight discriminative features? *Advances in Neural Information Processing Systems*, 34:2046–2059, 2021.
- [49] A. Shamir. A new theory of adversarial examples in machine learning (a non-technical extended abstract). *preprint*, 2021.
- [50] A. Shamir, O. Melamed, and O. BenShmuel. The dimpled manifold model of adversarial examples in machine learning. *arXiv preprint arXiv:2106.10151*, 2021.
- [51] K. Simonyan and A. Zisserman. Very deep convolutional networks for large-scale image recognition. In *International Conference on Learning Representations*, 2015.
- [52] C. Szegedy, W. Zaremba, I. Sutskever, J. Bruna, D. Erhan, I. Goodfellow, and R. Fergus. Intriguing properties of neural networks. In *International Conference on Learning Representations (ICLR)*, 2014.

- [53] R. Taori, A. Dave, V. Shankar, N. Carlini, B. Recht, and L. Schmidt. Measuring robustness to natural distribution shifts in image classification. In H. Larochelle, M. Ranzato, R. Hadsell, M. Balcan, and H. Lin, editors, *Advances in Neural Information Processing Systems*, volume 33, pages 18583–18599. Curran Associates, Inc., 2020. URL https://proceedings.neurips.cc/paper_files/paper/2020/file/d8330f857a17c53d217014ee776bfd50-Paper.pdf.
- [54] V. Tjeng, K. Xiao, and R. Tedrake. Evaluating robustness of neural networks with mixed integer programming. *arXiv preprint arXiv:1711.07356*, 2017.
- [55] F. Tramèr and D. Boneh. Adversarial training and robustness for multiple perturbations. *Advances in Neural Information Processing Systems*, 32, 2019.
- [56] F. Tramèr, N. Carlini, W. Brendel, and A. Madry. On adaptive attacks to adversarial example defenses. In H. Larochelle, M. Ranzato, R. Hadsell, M. Balcan, and H. Lin, editors, *Advances in Neural Information Processing Systems 33 (NeurIPS 2020)*, virtual, .
- [57] F. Tramèr, A. Kurakin, N. Papernot, I. J. Goodfellow, D. Boneh, and P. D. McDaniel. Ensemble adversarial training: Attacks and defenses. In *6th International Conference on Learning Representations, (ICLR 2018), Vancouver, BC, Canada*, .
- [58] D. Tsipras, S. Santurkar, L. Engstrom, A. Turner, and A. Madry. Robustness may be at odds with accuracy. In *7th International Conference on Learning Representations, ICLR 2019, New Orleans, LA, USA*.
- [59] G. Vardi, G. Yehudai, and O. Shamir. Gradient methods provably converge to non-robust networks, 2022.
- [60] Y. Wang, D. Zou, J. Yi, J. Bailey, X. Ma, and Q. Gu. Improving adversarial robustness requires revisiting misclassified examples. In *International Conference on Learning Representations*, 2020. URL <https://openreview.net/forum?id=rkl0g6EFwS>.
- [61] S.-A. Wegner. Lecture notes on high-dimensional spaces. *arXiv preprint arXiv:2101.05841*, 2021.
- [62] Y. Xu, Y. Sun, M. Goldblum, T. Goldstein, and F. Huang. Exploring and exploiting decision boundary dynamics for adversarial robustness, 2023.
- [63] G. Yang, T. Duan, J. E. Hu, H. Salman, I. Razenshteyn, and J. Li. Randomized smoothing of all shapes and sizes. In *International Conference on Machine Learning*, pages 10693–10705. PMLR, 2020.

A Bracketing Algorithm

The Bracketing Algorithm is a way to determine persistence of an image with respect to a given classifier, typically a DNN. The algorithm was implemented in Python for the experiments presented. The RANGEFINDER function is not strictly necessary, in that one could directly specify values of σ_{\min} and σ_{\max} , but we include it here so that the code could be automated by a user if so desired.

Algorithm 1 Bracketing algorithm for computing γ -persistence

```

function BRACKETING(image, classifier ( $\mathcal{C}$ ), numSamples,  $\gamma$ , maxSteps, precision)
  [ $\sigma_{\min}$ ,  $\sigma_{\max}$ ] = RANGEFINDER(image,  $\mathcal{C}$ , numSamples,  $\gamma$ )
  count = 1
  while count < maxSteps do
     $\sigma = \frac{\sigma_{\min} + \sigma_{\max}}{2}$ 
     $\gamma_{\text{new}} = \text{COMPUTE\_PERSISTENCE}(\sigma, \text{image}, \text{numSamples}, \mathcal{C})$ 
    if  $|\gamma_{\text{new}} - \gamma| < \text{precision}$  then
      return  $\sigma$ 
    else if  $\gamma_{\text{new}} > \gamma$  then
       $\sigma_{\min} = \sigma$ 
    else
       $\sigma_{\max} = \sigma$ 
    end if
    count = count + 1
  end while
  return  $\sigma$ 
end function

function RANGEFINDER(image,  $\mathcal{C}$ , numSamples,  $\gamma$ )
   $\sigma_{\min} = .5, \sigma_{\max} = 1.5$ 
   $\gamma_1 = \text{COMPUTE\_PERSISTENCE}(\sigma_{\min}, \text{image}, \text{numSamples}, \mathcal{C})$ 
   $\gamma_2 = \text{COMPUTE\_PERSISTENCE}(\sigma_{\max}, \text{image}, \text{numSamples}, \mathcal{C})$ 
  while  $\gamma_1 < \gamma$  or  $\gamma_2 > \gamma$  do
    if  $\gamma_1 < \gamma$  then
       $\sigma_{\min} = .5\sigma_{\min}$ 
       $\gamma_1 = \text{COMPUTE\_PERSISTENCE}(\sigma_{\min}, \text{image}, \text{numSamples}, \mathcal{C})$ 
    end if
    if  $\gamma_2 > \gamma$  then
       $\sigma_{\max} = 2\sigma_{\max}$ 
       $\gamma_2 = \text{COMPUTE\_PERSISTENCE}(\sigma_{\max}, \text{image}, \text{numSamples}, \mathcal{C})$ 
    end if
  end while
  return [ $\sigma_{\min}, \sigma_{\max}$ ]
end function

function COMPUTE_PERSISTENCE( $\sigma$ , image, numSamples,  $\mathcal{C}$ )
  sample =  $N(\text{image}, \sigma^2 I, \text{numSamples})$ 
   $\gamma_{\text{est}} = \frac{|\{\mathcal{C}(\text{sample}) = \mathcal{C}(\text{image})\}|}{\text{numSamples}}$ 
  return  $\gamma_{\text{est}}$ 
end function

```

B Convolutional neural networks used

In Table 1 we reported results on varying complexity convolutional neural networks. These networks consist of a composition of convolutional layers followed by a maxpool and fully connected layers. The details of the network layers are described in Table 3 where Ch is the number of channels in the convolutional components.

Table 3: Structure of the CNNs C-Ch used in Table 1

Layer	Type	Channels	Kernel	Stride	Output Shape
0	Image	1	NA	NA	(1, 28, 28)
1	Conv	Ch	(5, 5)	(1, 1)	(Ch, 24, 24)
2	Conv	Ch	(5, 5)	(1, 1)	(Ch, 20, 20)
3	Conv	Ch	(5, 5)	(1, 1)	(Ch, 16, 16)
4	Conv	Ch	(5, 5)	(1, 1)	(Ch, 12, 12)
5	Max Pool	Ch	(2, 2)	(2, 2)	(Ch, 6, 6)
7	FC	(Ch · 6 · 6, 256)	NA	NA	256
8	FC	(256, 10)	NA	NA	10

C Additional Figures

In this section we provide additional figures to demonstrate some of the experiments from the paper.

C.1 Additional figures from MNIST

In Figure 11 we begin with an image of a 1 and generate adversarial examples to the networks described in Section 4.1.1 via IGSM targeted at each class 2 through 9; plotted are the counts of output classifications by the DNN from samples from Gaussian distributions with increasing standard deviation; this complements Figure 3 in the main text. Note that the prevalence of the adversarial class falls off quickly in all cases, though the rate is different for different choices of target class.

We also show histograms corresponding to those in Figure 4 and the networks from Table 1. As before, for each image, we used IGSM to generate 9 adversarial examples (one for each target class) yielding a total of 1800 adversarial examples. In addition, we randomly sampled 1800 natural MNIST images. For each of the 3600 images, we computed 0.7-persistence. In Figure 12, we see histograms of these persistence values for the small fully connected networks with increasing levels of regularization. In each case, the test accuracy is relatively low and distortion relatively high. It should be noted that these high-distortion attacks against models with few effective parameters were inherently very stable – resulting in most of the “adversarial” images in these sets having higher persistence than natural images. This suggests a lack of the sharp conical regions which appear to characterize adversarial examples generated against more complicated models. In Figure 13 we see the larger fully connected networks from Table 1 and in Figure 14 we see some of the convolutional neural networks from Table 1.

C.2 Additional figures for ImageNet

In this section we show some additional figures of Gaussian sampling for ImageNet. In Figure 15 we see Gaussian sampling of an example of the class `indigo_bunting` and the frequency samplings for adversarial attacks of `goldfinch` toward `indigo_bunting` (classifier: `alexnet`, attack: PGD) and toward `alligator_lizard` (classifier: `vgg16`, attack: PGD). Compare the middle image to Figure 5, which is a similar adversarial attack but used the `vgg16` network classifier and the BIM attack. Results are similar. Also note that in each of the cases in Figure 15 the label of the original natural image never becomes the most frequent classification when sampling neighborhoods of the adversarial example.

In Figure 16, we have plotted γ -persistence along a straight line from a natural image to an adversarial image to it with differing values of the parameter γ . The γ -persistence in each case seems to change primarily when crossing the decision boundary. Interestingly, while the choice of γ does not make too much of a difference in the left subplot, it leads to more varying persistence values in the right subplot of Figure 16. This suggests that one should be careful not to choose too small of a γ value, and that persistence does indeed depend on the landscape of the decision boundary described by the classifier.

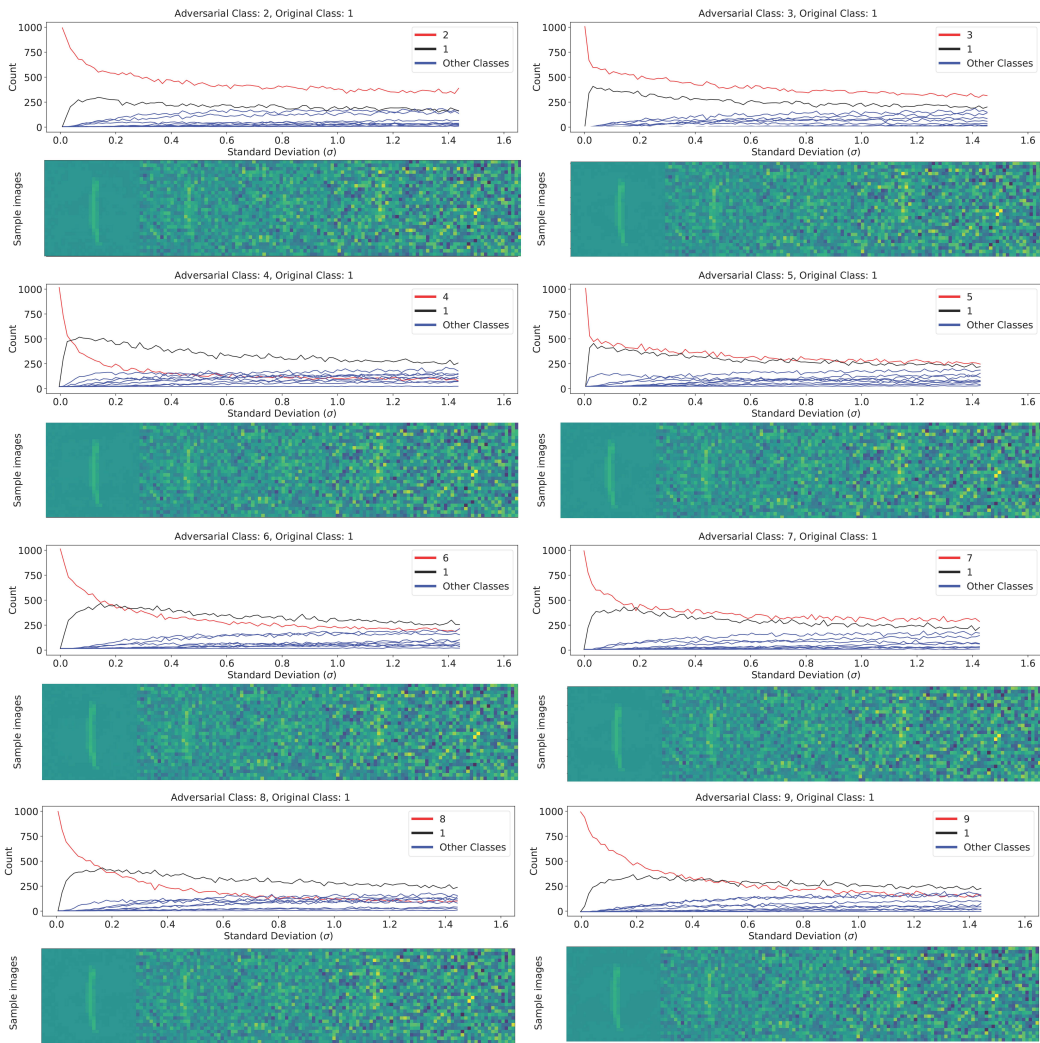


Figure 11: Frequency of each class in Gaussian samples with increasing standard deviations around adversarial attacks of an image of a 1 targeted at classes 2 through 9 on a DNN classifier generated using IGSM. The adversarial class is shown as a red curve. The natural image class (1) is shown in black. Bottoms show example sample images at different standard deviations.

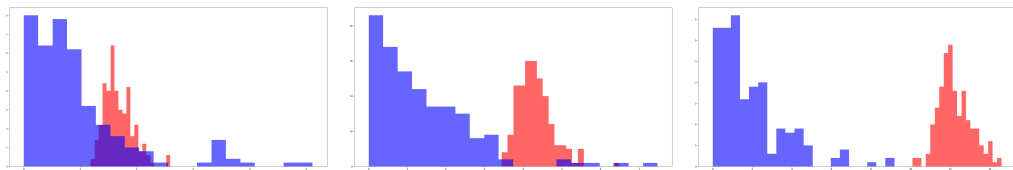


Figure 12: Histograms of 0.7-persistence for FC10-4 (smallest regularization, left), FC10-2 (middle), and FC10-0 (most regularization, right) from Table 1. Natural images are in blue, and adversarial images are in red. Note that these are plotted on different scales – higher regularization forces any "adversaries" to be very stable.

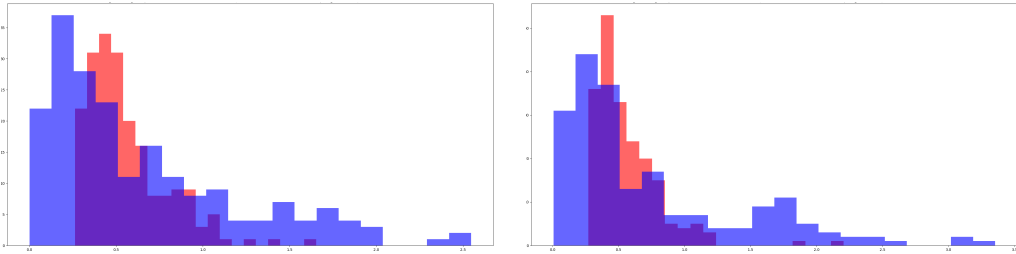


Figure 13: Histograms of 0.7-persistence for FC100-100-10 (left) and FC200-200-10 (right) from Table 1. Natural images are in blue, and adversarial images are in red.

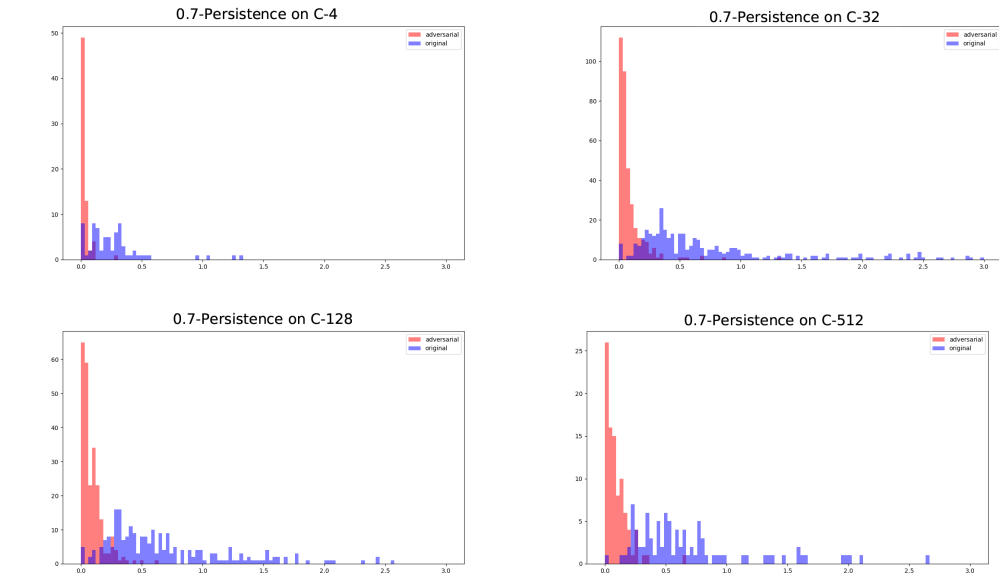


Figure 14: Histograms of 0.7-persistence for C-4 (top left), C-32 (top right), C-128 (bottom left), and C-512 (bottom right) from Table 1. Natural images are in blue and adversarial images are in red.

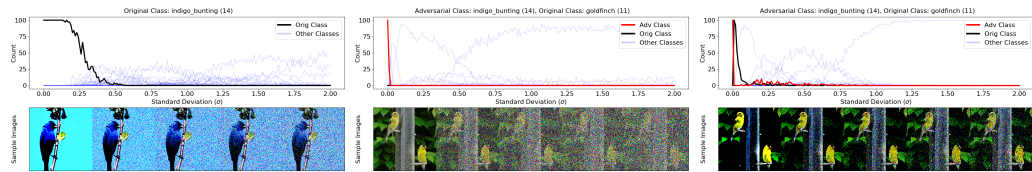


Figure 15: Frequency of each class in Gaussian samples with increasing variance around an indigo_bunting image (left), an adversarial example of the image in class goldfinch from Figure 5 targeted at the indigo_bunting class on a alexnet network attacked with PGD (middle), and an adversarial example of the goldfinch image targeted at the alligator_lizard class on a vgg16 network attacked with PGD (right). Bottoms show example sample images at different standard deviations.

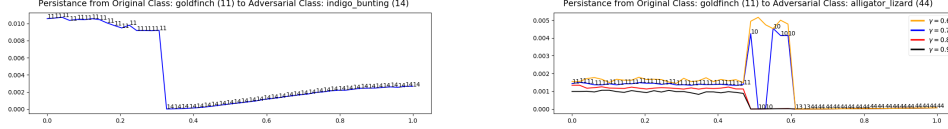


Figure 16: The γ -persistence of images along the straight line path from an image in class `goldfinch` (11) to an adversarial image generated with BIM in the class `indigo_bunting` (14) (left) and to an adversarial image generated with PGL in the class `alligator_lizard` (44) (right) on a vgg16 classifier with different values of γ . The classification of each image on the straight line is listed as a number so that it is possible to see the transition from one class to another. The vertical axis is γ -persistence and the horizontal axis is progress towards the adversarial image.

D Concentration of measures

We use Gaussian sampling with varying standard deviation instead of sampling the uniform distributions of balls of varying radius, denoted $U(B_r(0))$ for radius r and center 0. This is for two reasons. The first is that Gaussian sampling is relatively easy to do. The second is that the concentration phenomenon is different. This can be seen in the following proposition.

Proposition D.1. *Suppose $x \sim N(0, \sigma^2 I)$ and $y \sim U(B_r(0))$ where both points come from distributions on \mathbb{R}^n . For $\varepsilon < \sqrt{n}$ and for $\delta < r$ we find the following:*

$$\mathbb{P} \left[\left| \|x\| - \sigma\sqrt{n} \right| \leq \varepsilon \right] \geq 1 - 2e^{-\varepsilon^2/16} \quad (7)$$

$$\mathbb{P} \left[\left| \|y\| - r \right| \leq \delta \right] \geq 1 - e^{-\delta n/r} \quad (8)$$

Proof. This follows from [61, Theorems 4.7 and 3.7], which are the Gaussian Annulus Theorem and the concentration of measure for the unit ball, when taking account of varying the standard deviation σ and radius r , respectively. \square

The implication is that if we fix the dimension and let σ vary, the measures will always be concentrated near spheres of radius $\sigma\sqrt{n}$ and r , respectively, in a consistent way. In practice, Gaussian distributions seem to have a bit more spread, as indicated in Figure 17, which shows the norms of 100,000 points sampled from dimension $n = 784$ (left, the dimension of MNIST) and 5,000 points sampled from dimension $n = 196,608$ (right, the dimension of ImageNet).

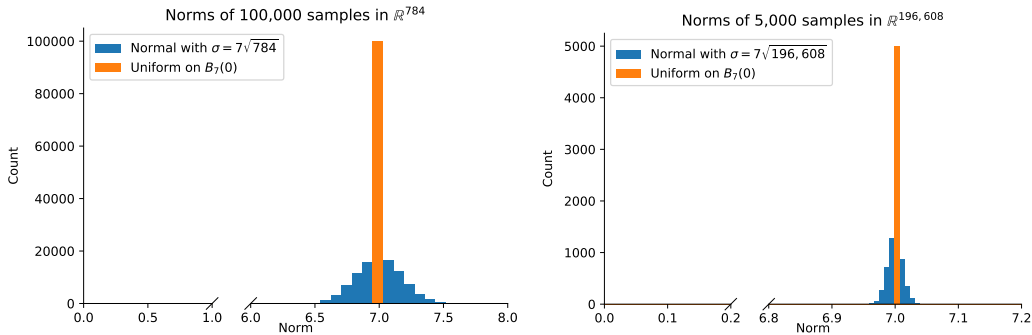


Figure 17: Comparison of the length of samples drawn from $U(B_7(0))$ and $N(0, 7\sqrt{n})$ for $n = 784$, the dimension of MNIST, (left) and $n = 196,608$, the dimension of ImageNet, (right).

E Licenses of Assets

We acknowledge the use of the following licensed materials: PyTorch (BSD License), MNIST (CC BY-SA 3.0 License), Imagenet (No License – downloaded in accordance with Princeton and Stanford University terms of access), and TorchAttacks (MIT License).